ATLAS NOTE

ATLAS-CONF-2012-166

December 5, 2012

Search for direct top squark pair production in final states with one isolated lepton, jets, and missing transverse momentum in $\sqrt{s} = 8$ TeV pp collisions using 13.0 fb^{-1} of ATLAS data

The ATLAS Collaboration

Abstract

A search is presented for direct top squark pair production in final states with one isolated electron or muon, jets, and missing transverse momentum in proton-proton collisions at a centre-of-mass energy of 8 TeV. The analysis is based on 13.0 fb^{-1} of data collected with the ATLAS detector at the LHC. The top squarks are assumed to decay to a top quark and the lightest supersymmetric particle (LSP) or to a bottom quark and a chargino, where the chargino decays to an on- or off-shell W boson and to the LSP. The data are found to be consistent with Standard Model expectations. Assuming both top squarks decay to a top quark and LSP, top squark masses between 225 and 560 GeV are excluded at 95% confidence level for massless LSPs, and top squark masses around 500 GeV are excluded for LSP masses up to 175 GeV. Assuming both top squarks decay to a bottom quark and chargino, top squark masses up to 350 GeV are excluded for massless LSPs and a chargino mass of 150 GeV.

ATLAS-CONF-2012-166
05 December 2012

1 Introduction

Weak scale Supersymmetry (SUSY) [1–9] is an extension to the Standard Model (SM) that provides a solution to the hierarchy problem by introducing supersymmetric partners for all SM particles. In the framework of a generic R-parity conserving minimal supersymmetric extension of the SM (MSSM) [10–14], SUSY particles are produced in pairs, and the lightest supersymmetric particle (LSP) is stable and can be a dark matter candidate. In a large variety of models, the LSP is the lightest neutralino, $\tilde{\chi}_1^0$, which only interacts weakly and thus escapes detection.

Light top squarks (stop) are suggested by naturalness arguments [15, 16]. In this analysis, one stop mass eigenstate ($\tilde{t}_1$) is assumed to be significantly lighter than the other squarks and the gluino. A search is presented for directly pair-produced stops. Two decay scenarios are considered. Either each $\tilde{t}_1$ decays to a top quark and the LSP ($\tilde{t}_1 \to t + \tilde{\chi}_1^0$), or each $\tilde{t}_1$ decays to a bottom quark and the lightest chargino ($\tilde{t}_1 \to b + \tilde{\chi}_1^{\pm}$), where the $\tilde{\chi}_1^{\pm}$ decays to an on- or off-shell W boson and to the LSP ($\tilde{\chi}_1^{\pm} \to W^{(*)} + \tilde{\chi}_1^0$).

The final state for the $\tilde{t}_1 \to t + \tilde{\chi}_1^0$ signal scenario is characterised by a top quark pair ($t\bar{t}$) produced in association with large missing transverse momentum (the magnitude of which is referred to as $E_{\mathrm{T}}^{\mathrm{miss}}$) from the two undetected LSPs. The final state for the $\tilde{t}_1 \to b + \tilde{\chi}_1^{\pm}$ signal scenario is similar: it contains two virtual or real W bosons, two b-jets and two LSPs, but the presence of $\tilde{\chi}_1^{\pm}$'s in the decay chain alters the kinematic properties.

Searches for direct stop pair production have been previously reported by the ATLAS [17–21] and CMS [22, 23] experiments, as well as by the CDF and D0 experiments assuming different SUSY mass spectra and decay modes (see for example Ref. [24] and [25]). Searches for stops via gluino pair ($\tilde{g}\tilde{g}$) production have been reported by the ATLAS [26–29] and CMS [30–32] collaborations.

This search is performed with the ATLAS detector [33], which has a solenoid, surrounding the inner tracking detector (ID), and a barrel and two endcap toroidal magnets supporting the muon spectrometer. The ID consists of silicon pixel, silicon microstrip, and transition radiation detectors and provides precision tracking of charged particles for pseudorapidity $|\eta| < 2.5$ [1]. The calorimeter placed outside the solenoid covers $|\eta| < 4.9$ and is composed of sampling electromagnetic and hadronic calorimeters with either liquid argon (LAr) or scintillating tiles as the active media. The muon spectrometer surrounds the calorimeters and consists of a system of precision tracking chambers in $|\eta| < 2.7$, and detectors for triggering in $|\eta| < 2.4$.

The analysis is based on data recorded by the ATLAS detector in 2012 corresponding to 13.0 fb^{-1} of integrated luminosity with the LHC operating at a pp centre-of-mass energy of 8 TeV. The data were collected requiring either a single-lepton (electron or muon) or an $E_{\mathrm{T}}^{\mathrm{miss}}$ trigger. The combined trigger efficiency is >98% for the lepton and $E_{\mathrm{T}}^{\mathrm{miss}}$ selection criteria applied in this analysis. Requirements that ensure the quality of beam conditions, detector performance and data are imposed.

2 Signal and Background Simulation

Monte Carlo (MC) simulation samples are used to aid in the description of the background and to model the SUSY signal. The MC samples are processed either with a full ATLAS detector simulation [34] based on the `Geant4` program [35] or a fast simulation based on the parameterization of the performance of the ATLAS electromagnetic and hadronic calorimeters [36]. The effect of multiple pp interactions in the same or nearby bunch crossing is also simulated. Production of top quark pairs is simulated

[1] ATLAS uses a right-handed coordinate system with its origin at the nominal interaction point in the centre of the detector and the z-axis along the beam pipe. Cylindrical coordinates (r, ϕ) are used in the transverse plane, ϕ being the azimuthal angle around the beam pipe. The pseudorapidity η is defined in terms of the polar angle θ by $\eta = -\ln\tan(\theta/2)$, and $\Delta R = \sqrt{(\Delta\eta)^2 + (\Delta\phi)^2}$

with PowHeg [37–39]. AcerMC [40] samples with various parameter settings are used to assess the uncertainties associated with initial and final state radiation (ISR/FSR). The parameter settings for the ISR/FSR variations have been obtained from a dedicated data study [41]. The MC@NLO generator is employed to assess the $t\bar{t}$ modelling uncertainty. A top quark mass of 172.5 GeV is used consistently. W and Z/γ^* production in association with jets are each modelled with SHERPA [42]. Diboson VV (WW, WZ, ZZ) production is simulated with SHERPA with up to three additional partons. Single top quark production is modelled with MC@NLO, and $t\bar{t}$ events produced in association with Z or W ($t\bar{t}+V$) are generated with MADGRAPH [43]. Next-to-leading order (NLO) PDFs CT10 [44] are used with all NLO MC samples. For all other samples, LO PDFs are used: MRSTmcal [45] with HERWIG [46], and CTEQ6L1 [47] with MADGRAPH. Fragmentation and hadronization for all samples are performed with PYTHIA [48], except for single top samples where HERWIG is used with JIMMY [49] for the underlying event. The $t\bar{t}$, single top and $t\bar{t}+V$ production cross sections are normalized to approximate next-to-next-to-leading order (NNLO) [50], next-to-next-to-leading-logarithmic accuracy (NLO+NNLL) [51–53] and NLO [54] calculations, respectively. QCD NNLO FEWZ [55] inclusive W and Z cross sections are used for the normalization of the W+jets and Z+jets processes. Expected diboson yields are normalized using NLO QCD predictions obtained with MCFM [56, 57].

The data modelling is improved for high jet multiplicities by reweighting the PowHeg $t\bar{t}$ sample to match the jet multiplicity distribution of ALPGEN. Furthermore, data modelling is improved by reweighting the SHERPA W simulation heavy-flavour quark p_{T} distributions to match the ALPGEN heavy-flavour samples.

Stop pair production with $\tilde{t}_1 \to t + \tilde{\chi}_1^0$ is modelled using HERWIG++ [58]. A signal grid is generated with a step size of 50 GeV (smaller step sizes close to the diagonal) both for the stop and LSP mass values. The $\tilde{t}_1$ is chosen to be mostly the partner of the right-handed top quark[2], and the $\tilde{\chi}_1^0$ to be almost a pure bino. Different hypotheses on the nature of the left/right mixing in the stop sector and the bino-like neutralino might lead to different acceptance values. In particular, if purely left-handed stops are considered the acceptance decreases by 10–50% depending on the model and selection criteria used. The acceptance is affected because the polarization of the quark changes as function of the field content of the supersymmetric particles, changing the boost of the lepton in the top quark decay.

Stop pair production with $\tilde{t}_1 \to b + \tilde{\chi}_1^{\pm}$ is modelled using MADGRAPH and PYTHIA. Two grids with different assumptions about the chargino-LSP mass difference are considered. In both grids the stop and LSP masses are varied. The first grid assumes gaugino universality, i.e. the chargino mass is fixed to two times the mass of the LSP ($m_{\tilde{\chi}_1^{\pm}} = 2 \times m_{\tilde{\chi}_1^0}$). In the other grid $m_{\tilde{\chi}_1^{\pm}} = 150$ GeV is fixed to be well above the present chargino mass limit from LEP [59]. The simplified model assumption of $\mathcal{B}(\tilde{t}_1 \to b\tilde{\chi}_1^{\pm}) = 100\%$ is less likely to be realized in the MSSM if $\tilde{t}_1 \to t + \tilde{\chi}_1^0/\tilde{\chi}_2^0$ decays are kinematically allowed. Depending on the left/right nature of the $\tilde{t}_1$ and the higgsino/bino mixture in the neutralino sector, the $b + \tilde{\chi}_1^{\pm}$ mode may still be dominant. Signal cross sections are calculated to NLO in the strong coupling constant, including the resummation of soft gluon emission at next-to-leading-logarithmic accuracy (NLO+NLL) [60–62]. The nominal cross section and the uncertainty are taken from an envelope of cross section predictions using different PDF sets and factorization and renormalization scales, as described in Ref. [63]. ISR specific uncertainties for the signal modelling are not included. The $\tilde{t}_1$ pair production cross section is (5.6 ± 0.8) pb for $m_{\tilde{t}_1} = 250$ GeV, and (0.025 ± 0.004) pb for $m_{\tilde{t}_1} = 600$ GeV.

3 Event Selection and Reconstruction

Events must pass basic quality criteria to reject detector noise and non-collision backgrounds [64, 65] and are required to have at least one reconstructed primary vertex associated with five or more tracks

[2] The stop mixing matrix is set with diagonal entries of 0.55 and off-diagonal entries of ±0.83.

with transverse momentum $p_{\mathrm{T}} > 0.4$ GeV. Events are retained if they contain exactly one muon [66] with $|\eta| < 2.4$ and $p_{\mathrm{T}} > 25$ GeV or one electron passing 'tight' [67] selection criteria with $|\eta| < 2.47$ and $p_{\mathrm{T}} > 25$ GeV. Leptons are required to be isolated from other particles. The scalar sum of the transverse momenta of tracks above 1 GeV within a cone of size $\Delta R < 0.2$ around the lepton candidate is required to be < 10% of the electron p_{T}, and < 1.8 GeV for a muon. Events are rejected if they contain additional leptons passing looser selection criteria and $p_{\mathrm{T}} > 10$ GeV. Jets are reconstructed from three-dimensional calorimeter energy clusters using the anti-k_t jet clustering algorithm [68] with a distance parameter of 0.4. Jet inputs (clusters) are calibrated for the effects of calorimeter non-compensation and inhomogeneities by weighting differently energy deposits arising from electromagnetic and hadronic showers using calibration factors derived from MC simulations and validated with data [69–72]. An additional jet energy calibration is subsequently applied to correct the jet energy response to the true hadron-level jet energy. The impact of additional collisions in the same or neighbouring bunch crossings is also taken into account using offset corrections derived as a function of the average number of interactions per bunch crossing $\langle\mu\rangle$ and of the number of primary vertices. Events with four or more jets are selected with $|\eta| < 2.5$ and $p_{\mathrm{T}} > 80, 60, 40, 25$ GeV, respectively. At least one jet needs to be identified as a b-jet. Jets containing a b-hadron decay (b-jets) are identified using the 'MV1' b-tagging algorithm [73–76] which exploits both impact parameter and secondary vertex information. An operating point is employed corresponding to an average 75% b-tagging efficiency and a < 2% misidentification rate for light-quark/gluon jets for jets with $p_{\mathrm{T}} > 20$ GeV and $|\eta| < 2.5$ in $t\bar{t}$ MC events.

To resolve overlaps between reconstructed jets and electrons, jets within a distance of $\Delta R < 0.2$ of an electron candidate are rejected. Furthermore, any lepton candidate with a distance $\Delta R < 0.4$ to the closest remaining jet is discarded. The measurement of $E_{\mathrm{T}}^{\mathrm{miss}}$ is based on the transverse momenta of all electron and muon candidates, all jets after overlap removal, and all calorimeter energy clusters not associated to such objects.

3.1 Signal Regions

Six signal regions (SRs) are defined in order to optimize the sensitivity for different stop and LSP masses. The two tightest SRs D and E from the 2011 $\tilde{t}_1 \to t + \tilde{\chi}_1^0$ analysis [20] have been retained for comparison. Three SRs (labeled SRtN 1–3) have been optimized for the top LSP decay scenario exploiting the discrimination power of all the variables studied. Each of these three SRs was optimized for a specific mass region: SRtN1 for models where $m_{\tilde{t}_1} \gtrsim m_t + m_{\tilde{\chi}_1^0}$ (close to the diagonal in the exclusion plot), SRtN2 for models with high $m_{\tilde{\chi}_1^0}$, and SRtN3 for very high $m_{\tilde{t}_1}$. The last SR (labelled SRbC) is used for the bottom chargino decay scenario.

All five $\tilde{t}_1 \to t + \tilde{\chi}_1^0$ SRs require a selection on the 3-jet mass m_{jjj} of the hadronically decaying top quark to specifically reject the $t\bar{t}$ background where both W bosons from the top quarks decay leptonically. The jet-jet pair with an invariant mass above 60 GeV which has the smallest ΔR is selected to form the hadronic W boson. The mass m_{jjj} is reconstructed from a third jet closest in ΔR to the hadronic W boson momentum vector and 130 GeV $< m_{jjj} <$ 205 GeV is required. To reduce background from dileptonic $t\bar{t}$ events with a hadronic τ in the final state, the selection in SRbC vetoes events that contain an isolated track with $p_{\mathrm{T}} > 10$ GeV which passes basic track quality criteria and does not match the selected lepton. The isolation criterion requires no additional track with $p_{\mathrm{T}} > 3$ GeV in a cone of $\Delta R < 0.4$ around the candidate track.

For increasing stop mass and increasing mass difference between the stop and the LSP the requirements are tightened on $E_{\mathrm{T}}^{\mathrm{miss}}$, on the ratio $E_{\mathrm{T}}^{\mathrm{miss}}/\sqrt{H_{\mathrm{T}}}$, where H_{T} is the scalar sum of the momenta of the four selected jets, and on the transverse mass[3] m_{T}. Requirements are also tightened on two variants

[3]The transverse mass is defined as $m_{\mathrm{T}}^2 = 2p_{\mathrm{T}}^{\mathrm{lep}} E_{\mathrm{T}}^{\mathrm{miss}}(1 - \cos(\Delta\phi))$, where $\Delta\phi$ is the azimuthal angle between the lepton and missing momentum direction.

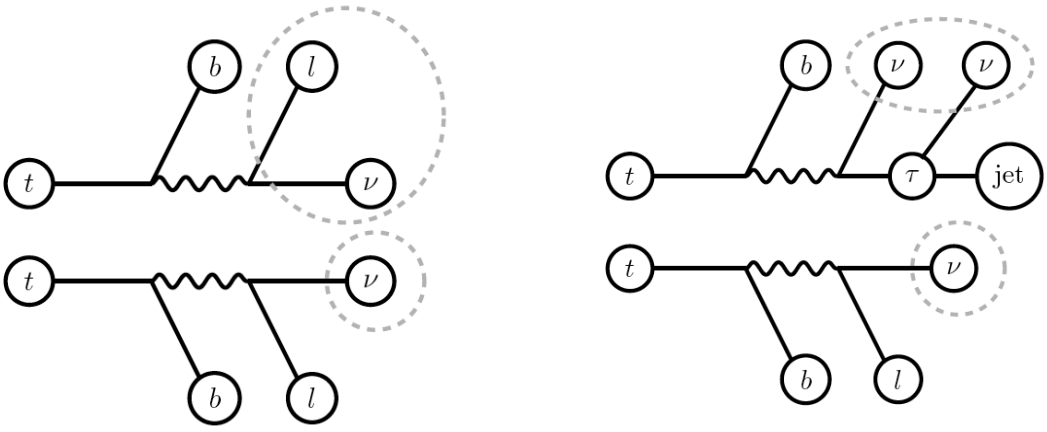

Figure 1: Illustration of the am_{T2} (left) and m_{T2}^{τ} (right) variables used to discriminate against dileptonic $t\bar{t}$ background where one lepton is lost (left) or decays into a hadronically decaying τ (right).

of the variable m_{T2} [77] to further reduce the dileptonic $t\bar{t}$ background. The first variant is a form of asymmetric m_{T2} (am_{T2}) [78–80] in which the daughter particle is the W boson for the branch with the lost lepton and the neutrino for the branch with the observed charged lepton. For dileptonic $t\bar{t}$ events with a lost lepton, am_{T2} is constructed to be bounded by the top quark mass, whereas new physics can exceed this bound. The second m_{T2} variant (m_{T2}^{τ}) is designed for events with a hadronic τ lepton by using the W bosons as parent particles and the 'τ-jet' as a visible particle on one branch and the observed lepton for the other branch. For both m_{T2} variables, the b-jets are chosen based on the highest b-tagging weight. For m_{T2}^{τ}, the 'τ-jet' is the highest p_{T} jet excluding the chosen b-jets. Figure 1 illustrates these two m_{T2} variables.

Furthermore, requirements on a minimal azimuthal (transverse) separation between the leading or sub-leading jet and the missing transverse momentum direction ($\Delta\phi(\mathrm{jet}_{1,2}, \vec{p}_{\mathrm{T}}^{\,\mathrm{miss}})$) are used to suppress the backgrounds. Table 1 gives an overview of the SR requirements and the resulting product of the acceptance and reconstruction efficiency for selected benchmark points. The numbers of observed events in each signal region after applying all selection criteria are given in Tables 2 through 7.

3.2 Background Modelling

The dominant background arises from dileptonic $t\bar{t}$ events in which one of the leptons is not identified, is outside the detector acceptance, or is a hadronically decaying τ lepton. In all these cases, the $t\bar{t}$ decay products include two or more high-p_{T} neutrinos, resulting in large $E_{\mathrm{T}}^{\mathrm{miss}}$ and large m_{T}.

For each SR two control regions (CRs) enriched in $t\bar{t}$ events (TCR) and W+jets events (WCR) are defined to normalize the corresponding backgrounds using data. Both CRs differ from the corresponding signal region by the m_{T} requirement which is set to 60 GeV $< m_{\mathrm{T}} <$ 90 GeV. The WCR also has a b-jet veto instead of a b-jet requirement to reduce the $t\bar{t}$ contamination. Moreover the requirements on $E_{\mathrm{T}}^{\mathrm{miss}}$, am_{T2} and m_{T2}^{τ} are slightly loosened for the CRs corresponding to SRs tN2 and tN3. All the other SR requirements are unchanged in the corresponding CRs. Top production accounts for 60–80% of events in the top control regions and W+jets production for 70–90% in the W control regions. The maximum signal contamination for all grid points studied is 10% for the $\tilde{t}_1 \to t+\tilde{\chi}_1^0$ CRs and 8% for the $\tilde{t}_1 \to b+\tilde{\chi}_1^{\pm}$ CRs.

For each signal region, a simultaneous fit to the signal region and the two associated control regions is performed to normalize the $t\bar{t}$ and W+jets background estimates as well as determine or limit a potential signal contribution. The multijet background, which mainly originates from jets misidentified as leptons,

Table 1: Selection requirements defining the SRs. The last row gives the expected acceptance times efficiency for the $\tilde{t}_1 \rightarrow t + \tilde{\chi}_1^0$ benchmark models: $m(\tilde{t}_1,\tilde{\chi}_1^0) = (250, 50)$ GeV for SRtN1, $m(\tilde{t}_1,\tilde{\chi}_1^0) = (500, 200)$ GeV for SRtN2, and $m(\tilde{t}_1,\tilde{\chi}_1^0) = (650, 1)$ GeV for SRtN3, as well as for the $\tilde{t}_1 \rightarrow b + \tilde{\chi}_1^{\pm}$ benchmark model $m(\tilde{t}_1,\tilde{\chi}_1^0,\tilde{\chi}_1^{\pm}) = (350, 150, 300)$ GeV for SRbC.

Requirement	SRD	SRE	SRtN1	SRtN2	SRtN3	SRbC
$\Delta\phi(j_1, \vec{p}_{\mathrm{T}}^{\,\mathrm{miss}}) >$	0.8	0.8	0.8	-	0.8	0.8
$\Delta\phi(j_2, \vec{p}_{\mathrm{T}}^{\,\mathrm{miss}}) >$	0.8	0.8	0.8	0.8	0.8	0.8
$E_{\mathrm{T}}^{\mathrm{miss}}$ [GeV] >	225	275	150	200	225	150
$E_{\mathrm{T}}^{\mathrm{miss}}/\sqrt{H_{\mathrm{T}}}$ [GeV$^{1/2}$] >	11	11	8	13	11	7
m_{T} [GeV] >	130	140	140	140	180	120
m_{T} [GeV] <	-	-	250	-	-	-
am_{T2} [GeV] >	-	-	-	170	200	-
m_{T2}^{τ} [GeV] >	-	-	-	-	120	-
$N^{\mathrm{iso-trk}} = 0$	-	-	-	-	-	Yes
$A \times \varepsilon$ benchmark point	-	-	0.06%	0.9%	2.8%	0.7%

is estimated using the matrix method [81] and is found to be negligible. Other background contributions (VV, $t\bar{t} + V$, single top) are estimated using MC simulation normalized to the theoretical cross sections. The Z+jets background is found to be negligible in all SRs and CRs. Systematic uncertainties are treated as nuisance parameters in the profile likelihood fit [82] with Gaussian probability density functions.

Agreement within experimental uncertainties is observed between data and the SM prediction before the fit as shown in Fig. 2 for the $E_{\mathrm{T}}^{\mathrm{miss}}$ distributions in the TCR-SRtN1 and TCR-SRbC, and the m_{T} and jet multiplicity distributions for looser preselection requirements. Figure 3 shows data and SM predictions before the fit for the signal selections.

4 Systematics

The dominant sources of systematic uncertainties in the fitted $t\bar{t}$ background estimates arise from theoretical and MC modelling uncertainties affecting the fiducial acceptance differences between CRs and SRs. They are determined by comparing different generators (`MC@NLO` and `PowHeg`), different showering models (`HERWIG` and `PYTHIA`) and by varying ISR/FSR parameters, and amount to 10–30% on the extrapolation of the fitted event yields from the control to the signal regions. The corresponding theoretical and MC modelling uncertainties on the fitted W+jets background estimates amount to 10–20% due to generator comparison (`SHERPA` and `ALPGEN`). An additional uncertainty of 30% is assigned to the W+heavy-flavour component to describe its relative cross section uncertainty with respect to the inclusive W+jets background. Electroweak single top production is associated with an 8% theoretical uncertainty [51–53] and $t\bar{t} + V$ background with a 30% uncertainty [54]. The uncertainty on the multijet background is based on the matrix method, with an uncertainty of 70%. Both the diboson and Z+jets background estimates are assigned an uncertainty of 100%.

Experimental uncertainties affect the signal and background yields estimated from MC events and are dominated by the uncertainties in jet energy scale, jet energy resolution, b-tagging, and modelling of

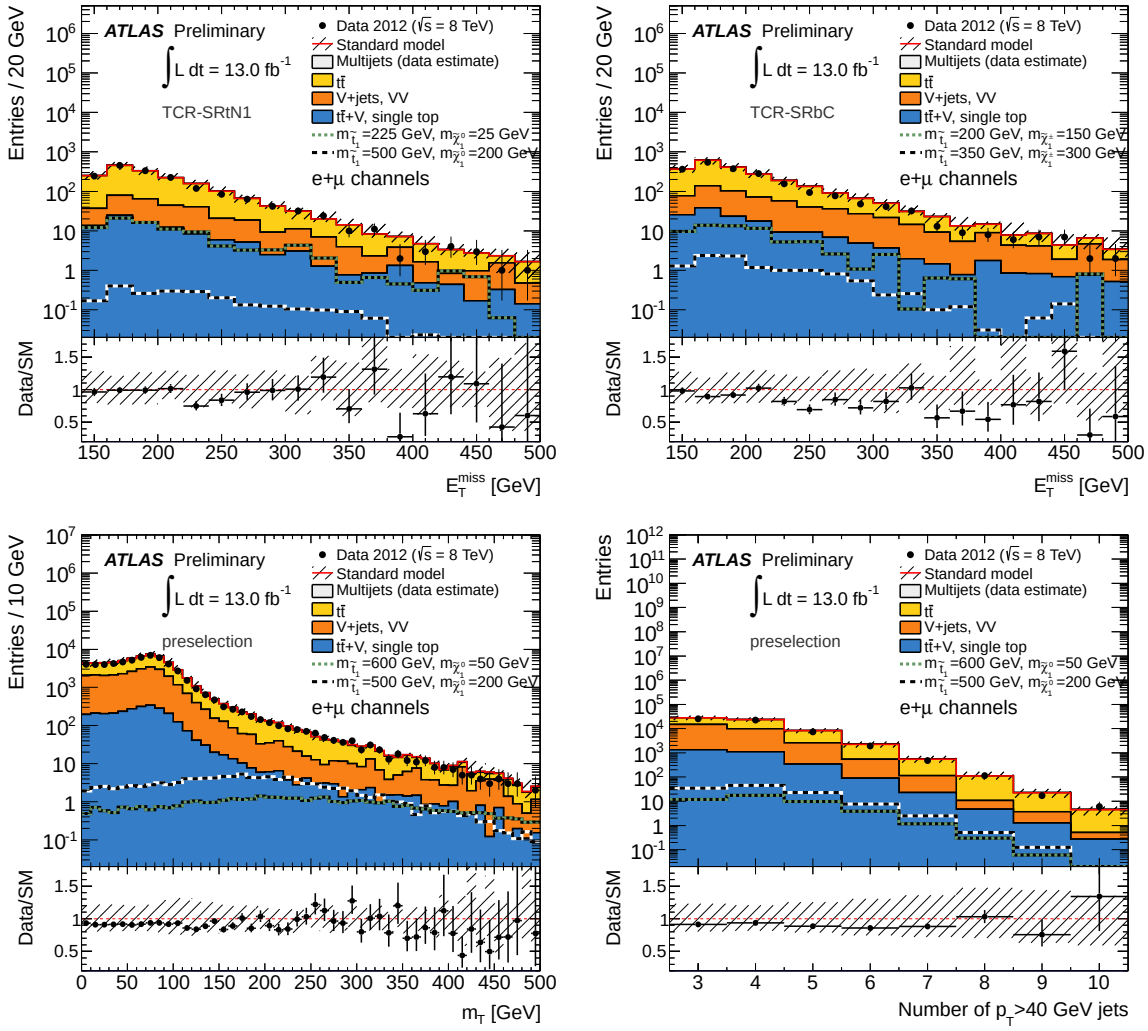

Figure 2: Comparison of data with MC predictions in control regions (top) and at preselection stage (bottom). Top: $E_{\mathrm{T}}^{\mathrm{miss}}$ distributions for TCR-SRtN1 (left) and TCR-SRbC (right). Bottom: m_{T} (left) and jet multiplicity (right) distributions for a preselection consisting of the standard trigger, data quality, lepton, ≥ 4 jets ($p_{\mathrm{T}} > 80, 60, 40, 25\,\mathrm{GeV}$, respectively), and $E_{\mathrm{T}}^{\mathrm{miss}} > 100\,\mathrm{GeV}$ requirements. Different stop benchmark models are shown in the four plots. The top left and two bottom plots show $\tilde{t}_1 \rightarrow t + \tilde{\chi}_1^0$ models, while the top right plot shows $\tilde{t}_1 \rightarrow b + \tilde{\chi}_1^{\pm}$ models with $m_{\tilde{\chi}_1^{\pm}} = 2 \times m_{\tilde{\chi}_1^0}$ (the legend shows $m_{\tilde{t}_1}$ and $m_{\tilde{\chi}_1^{\pm}}$ only). Signal histograms are not stacked. All plots show the combined electron and muon channels, before normalization fits. Hatched areas indicate the combined uncertainty due to MC sample size and the jet energy scale.

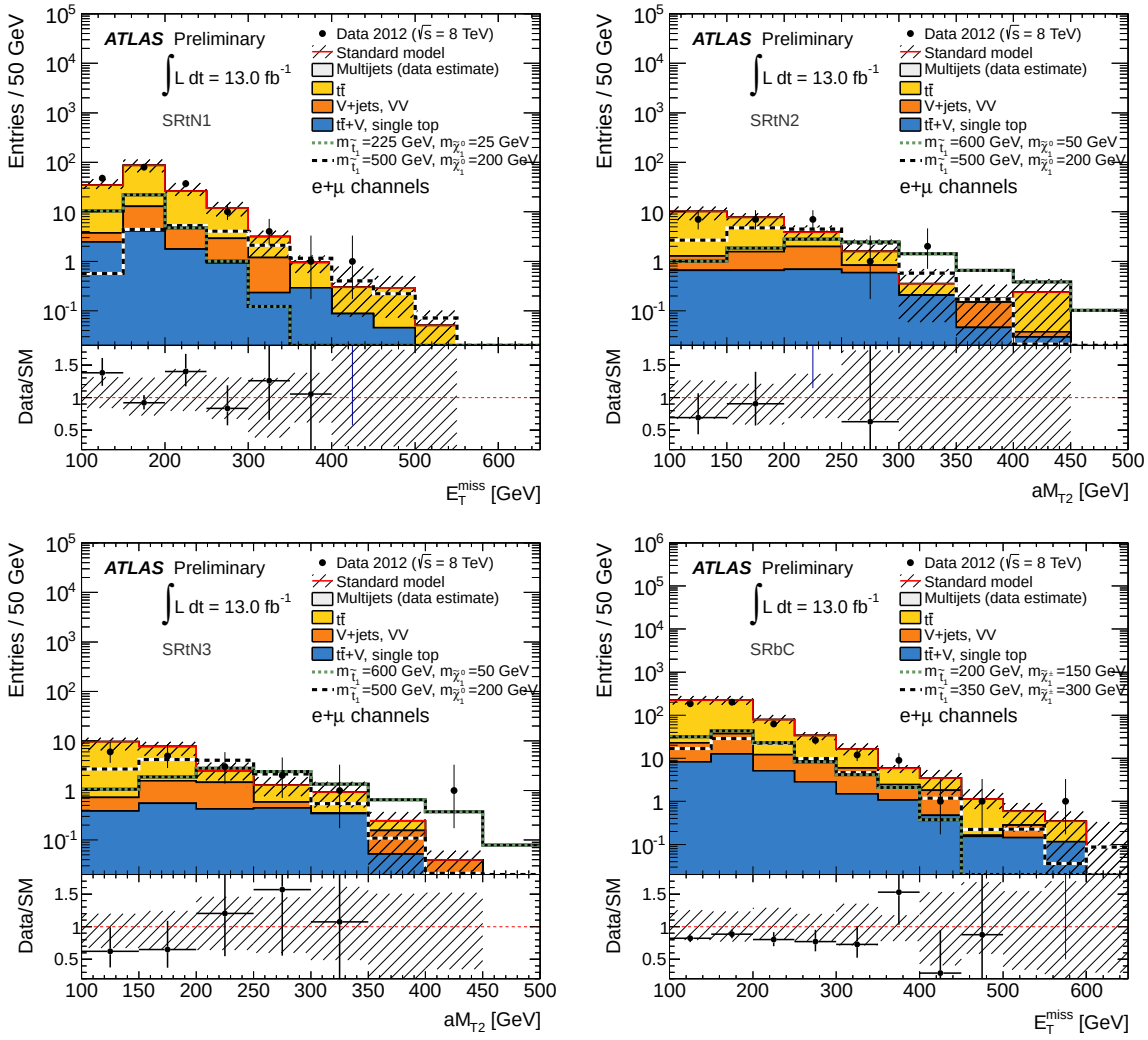

Figure 3: Comparison of data with MC predictions imposing the various signal event selections requirements except for the cut on the shown variable. Top left: $E_{\mathrm{T}}^{\mathrm{miss}}$ distributions for SRtN1. Top right: am_{T2} distribution for SRtN2. Bottom left: am_{T2} distribution for SRtN3. Bottom right: $E_{\mathrm{T}}^{\mathrm{miss}}$ distributions for SRbC. Different stop benchmark models are shown in the four plots. The two models shown for SRbC are $\tilde{t}_1 \rightarrow b + \tilde{\chi}_1^{\pm}$ decays with $m_{\tilde{\chi}_1^{\pm}} = 2 \times m_{\tilde{\chi}_1^0}$ (the legend shows $m_{\tilde{t}_1}$ and $m_{\tilde{\chi}_1^{\pm}}$ only), while the other three plots show models with $\tilde{t}_1 \rightarrow t + \tilde{\chi}_1^0$ decays. Signal histograms are not stacked. All plots show the combined electron and muon channels, before normalization fits. Hatched areas indicate the combined uncertainty due to MC sample size and the jet energy scale.

Regions	SRbC	WCR-SRbC	TCR-SRbC
$t\bar{t}$	260 ± 38	306 ± 94	1473 ± 99
$t\bar{t}+V$	8.9 ± 3.0	2.0 ± 0.8	10 ± 3
W+jets	37 ± 10	1231 ± 113	381 ± 78
Single top	15 ± 4	30 ± 11	140 ± 33
Z+jets, VV, multijet	4.9 ± 3.1	62 ± 38	67 ± 40
Total background	325 ± 36	1631 ± 42	2071 ± 47
Signal benchmark $m(\tilde{t}_1,\tilde{\chi}_1^0,\tilde{\chi}_1^\pm) = (200, 75, 150)$	81.4		
Signal benchmark $m(\tilde{t}_1,\tilde{\chi}_1^0,\tilde{\chi}_1^\pm) = (350, 150, 300)$	69.7		
Observed events	314	1631	2071

Table 2: Numbers of observed events in signal region bC and the two associated background control regions, as well as their estimated values and all (statistic and systematic) uncertainties from a fit to the control regions only, for the combined electron and muon channels. The expected numbers of signal events for two $\tilde{t}_1 \to b\tilde{\chi}_1^\pm$ benchmark points are listed for comparison. The central values of the fitted sum of backgrounds in the control regions agree with the observations by construction. The uncertainty on the total background estimate can be smaller than some of the individual uncertainties due to anticorrelations.

multiple pp interactions. Uncertainties related to the trigger and lepton reconstruction and identification (momentum and energy scales, resolutions and efficiencies) give smaller contributions. Other small uncertainties are due to the integrated luminosity (3.6% measured using techniques similar to those in [83, 84]), and the limited MC and data statistics. Systematic uncertainties due to the isolated track veto have been studied, including its pileup dependence, and found to be negligible.

5 Results

Table 2 (Tables 3 to 7) shows the result of the background fit to the $\tilde{t}_1 \to b + \tilde{\chi}_1^\pm$ ($\tilde{t}_1 \to t + \tilde{\chi}_1^0$) control regions, the fitted $t\bar{t}$ and W+jets event yields extrapolated to the signal region, the other background estimates, the numbers of observed events, and the numbers of expected events for signal benchmark models. The fitted W+jets and $t\bar{t}$ backgrounds are compatible with MC predictions within uncertainties. To assess the agreement between SM expectation and observation in the signal regions simultaneous fits including the signal and control regions are performed for each SR. The p_0-values obtained for the background-only hypothesis are given in Table 8. The observed numbers of events are compatible with the background-only hypothesis.

One-sided exclusion limits are derived using the CL_s method [85], based on the same simultaneous fit (including signal and control regions) but taking the predicted signal contamination in the control regions into account. To obtain the best expected combined exclusion limit, a mapping in the stop-LSP mass plane is constructed by selecting the signal region with the lowest expected CL_s value for each grid point. For the $\tilde{t}_1 \to t + \tilde{\chi}_1^0$ decay scenario the region of excluded stop and LSP masses is shown in Fig. 4. Stop masses are excluded between 225 GeV and 560 GeV for massless LSPs, and stop masses around 500 GeV are excluded along a line which approximately corresponds to LSP masses up to 175 GeV. These values are derived from the $-1\,\sigma^{\text{SUSY}}_{\text{theory}}$ observed limit contour. SRtN1 is responsible for the search sensitivity at the lowest stop masses and also close to the diagonal, SRtN2 provides the best sensitivity up to stop masses of about 600 GeV, and SRtN3 takes over for higher stop masses. For the $\tilde{t}_1 \to b\tilde{\chi}_1^\pm$ decay the exclusion limits are shown in Fig. 5 for $m_{\tilde{\chi}_1^\pm} = 150$ GeV and Fig. 6 for $m_{\tilde{\chi}_1^\pm} = 2 \times m_{\tilde{\chi}_1^0}$. Stop masses are excluded up to 350 GeV for massless LSPs and $m_{\tilde{\chi}_1^\pm} = 150$ GeV. For the $m_{\tilde{\chi}_1^\pm} = 2 \times m_{\tilde{\chi}_1^0}$ scenario, stop

Regions	SRD	WCR-SRD	TCR-SRD
$t\bar{t}$	25 ± 5	51 ± 21	217 ± 25
$t\bar{t}+V$	2.8 ± 1.1	0.6 ± 0.3	2.2 ± 0.8
W+jets	3.4 ± 1.1	168 ± 28	53 ± 13
Single top	0.9 ± 0.4	4.6 ± 3.1	24 ± 8
Z+jets, VV, multijet	1.0 ± 1.0	8.5 ± 6.7	11 ± 8
Total background	34 ± 5	232 ± 15	306 ± 18
Observed events	40	232	306

Table 3: Numbers of observed events in signal region D and the two associated background control regions, as well as their estimated values and all (statistic and systematic) uncertainties from a fit to the control regions only, for the combined electron and muon channels. The central values of the fitted sum of backgrounds in the control regions agree with the observations by construction. The uncertainty on the total background estimate can be smaller than some of the individual uncertainties due to anticorrelations.

Regions	SRE	WCR-SRE	TCR-SRE
$t\bar{t}$	11 ± 3	25 ± 12	104 ± 18
$t\bar{t}+V$	1.5 ± 0.6	0.3 ± 0.2	1.2 ± 0.5
W+jets	1.0 ± 0.5	75 ± 11	22 ± 6
Single top	0.3 ± 0.7	1.0 ± 0.9	11.4 ± 4.4
Z+jets, VV, multijet	0.3 ± 0.6	3.8 ± 3.4	6.1 ± 4.7
Total background	14 ± 3	105 ± 9	144 ± 13
Observed events	21	105	144

Table 4: Numbers of observed events in signal region E and the two associated background control regions, as well as their estimated values and all (statistic and systematic) uncertainties from a fit to the control regions only, for the combined electron and muon channels. The central values of the fitted sum of backgrounds in the control regions agree with the observations by construction. The uncertainty on the total background estimate can be smaller than some of the individual uncertainties due to anticorrelations.

Regions	SRtN1	WCR-SRtN1	TCR-SRtN1
$t\bar{t}$	104 ± 17	291 ± 89	1357 ± 68
$t\bar{t}+V$	4.6 ± 1.7	1.7 ± 0.7	8.1 ± 2.7
W+jets	11 ± 3	553 ± 75	175 ± 41
Single top	2.9 ± 1.4	21 ± 10	89 ± 22
Z+jets, VV, multijet	1.9 ± 1.5	31 ± 21	32 ± 21
Total background	125 ± 17	897 ± 41	1661 ± 43
Signal benchmark $m(\tilde{t}_1,\tilde{\chi}_1^0) = (250, 50)$	46.2		
Signal benchmark $m(\tilde{t}_1,\tilde{\chi}_1^0) = (500, 200)$	17.7		
Signal benchmark $m(\tilde{t}_1,\tilde{\chi}_1^0) = (650, 1)$	2.9		
Observed events	133	897	1661

Table 5: Numbers of observed events in signal region tN1 and the two associated background control regions, as well as their estimated values and all (statistic and systematic) uncertainties from a fit to the control regions only, for the combined electron and muon channels. The expected numbers of signal events for three $\tilde{t}_1 \to t\tilde{\chi}_1^0$ benchmark points are listed for comparison. The central values of the fitted sum of backgrounds in the control regions agree with the observations by construction. The uncertainty on the total background estimate can be smaller than some of the individual uncertainties due to anticorrelations.

Regions	SRtN2	WCR-SRtN2	TCR-SRtN2
$t\bar{t}$	5.4 ± 1.7	27 ± 12	111 ± 17
$t\bar{t}+V$	1.5 ± 0.7	0.3 ± 0.1	1.1 ± 0.4
W+jets	1.6 ± 0.7	112 ± 19	36 ± 10
Single top	0.5 ± 0.2	2.7 ± 2.4	15 ± 5
Z+jets, VV, multijet	0.6 ± 0.7	4.3 ± 3.8	6.6 ± 5.1
Total background	9.6 ± 1.5	147 ± 12	169 ± 12
Signal benchmark $m(\tilde{t}_1,\tilde{\chi}_1^0) = (250, 50)$	1.6		
Signal benchmark $m(\tilde{t}_1,\tilde{\chi}_1^0) = (500, 200)$	10.6		
Signal benchmark $m(\tilde{t}_1,\tilde{\chi}_1^0) = (650, 1)$	5.9		
Observed events	12	147	169

Table 6: Numbers of observed events in signal region tN2 and the two associated background control regions, as well as their estimated values and all (statistic and systematic) uncertainties from a fit to the control regions only, for the combined electron and muon channels. The expected numbers of signal events for three $\tilde{t}_1 \to t\tilde{\chi}_1^0$ benchmark points are listed for comparison. The central values of the fitted sum of backgrounds in the control regions agree with the observations by construction. The uncertainty on the total background estimate can be smaller than some of the individual uncertainties due to anticorrelations.

Regions	SRtN3	WCR-SRtN3	TCR-SRtN3
$t\bar{t}$	1.9 ± 0.8	25 ± 11	112 ± 16
$t\bar{t} + V$	1.0 ± 0.4	0.3 ± 0.1	1.5 ± 0.5
W+jets	1.2 ± 0.4	133 ± 20	51 ± 13
Single top	0.3 ± 0.5	3.2 ± 1.7	21 ± 6
Z+jets, VV, multijet	0.0 ± 0.3	7.5 ± 5.9	9.2 ± 6.8
Total background	4.3 ± 1.1	169 ± 14	195 ± 12
Signal benchmark $m(\tilde{t}_1, \tilde{\chi}_1^0) = (250, 50)$	0.3		
Signal benchmark $m(\tilde{t}_1, \tilde{\chi}_1^0) = (500, 200)$	6.9		
Signal benchmark $m(\tilde{t}_1, \tilde{\chi}_1^0) = (650, 1)$	5.0		
Observed events	8	169	195

Table 7: Numbers of observed events in signal region tN3 and the two associated background control regions, as well as their estimated values and all (statistic and systematic) uncertainties from a fit to the control regions only, for the combined electron and muon channels. The expected numbers of signal events for three $\tilde{t}_1 \to t\tilde{\chi}_1^0$ benchmark points are listed for comparison. The central values of the fitted sum of backgrounds in the control regions agree with the observations by construction. The uncertainty on the total background estimate can be smaller than some of the individual uncertainties due to anticorrelations.

p_0-values	SRD	SRE	SRtN1	SRtN2	SRtN3	SRbC
	0.20	0.18	0.33	0.24	0.15	0.42

Table 8: Compatibility of the observed numbers of events with the background-only hypothesis, represented by the p_0-values obtained from the discovery fit setup (see text).

masses are excluded along the diagonal where $m_{\tilde{t}_1} \sim m_t + m_{\tilde{\chi}_1^0}$. The results of this search significantly extend previous stop mass limits.

Limits on beyond-SM contributions are derived from the same simultaneous fit but without signal model-dependent inputs (i.e. without signal contamination in the control regions, and without experimental and theoretical signal systematic uncertainties). The resulting limits are shown in Table 9.

6 Conclusion

In summary, a search for stop pair production is presented in final states with one isolated lepton, jets, and missing transverse momentum in $\sqrt{s} = 8$ TeV pp collisions corresponding to 13.0 fb^{-1} of ATLAS 2012 data. The stops are assumed to decay each to a top quark and a long-lived undetected neutral particle or to a bottom quark and a chargino. No significant excess of events above the rate predicted by the Standard Model is observed and 95% CL upper limits are set on the stop mass in the stop-LSP mass plane, significantly extending previous stop mass limits.

References

[1] H. Miyazawa, *Baryon Number Changing Currents*, Prog. Theor. Phys. **36 (6)** (1966) 1266–1276.

[2] R. Ramond, *Dual Theory for Free Fermions*, Phys. Rev. **D3** (1971) 2415–2418.

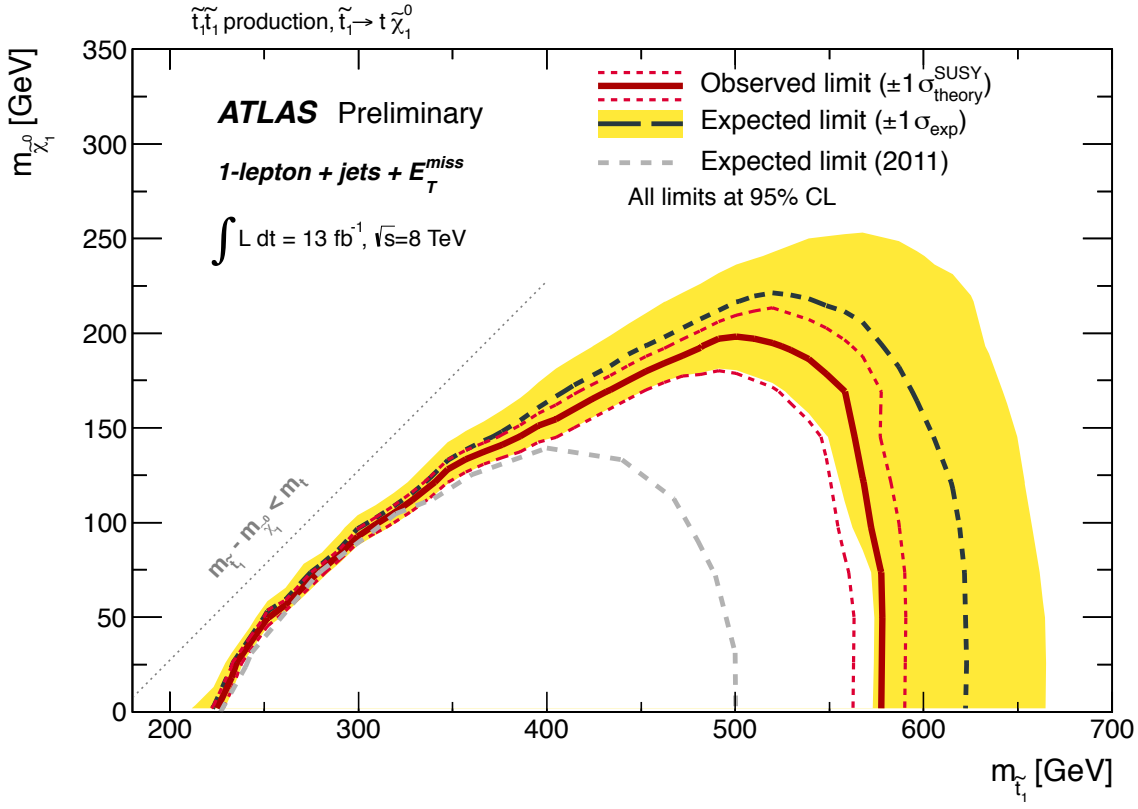

Figure 4: Expected (black dashed) and observed (red solid) 95% CL excluded region (under the curve) in the plane of $m_{\tilde{\chi}_1^0}$ vs. $m_{\tilde{t}_1}$, assuming $\mathcal{B}(\tilde{t}_1 \rightarrow t\tilde{\chi}_1^0) = 100\%$. All uncertainties except the theoretical signal cross section uncertainties are included. The contours of the yellow band around the expected limit are the $\pm 1\,\sigma$ results. The dotted red lines around the observed limit illustrate the change in the observed limit as the nominal signal cross section is scaled up and down by the theoretical uncertainty. For comparison the light grey dashed line shows the corresponding 2011 ATLAS expected limit from the stop 1-lepton search [20].

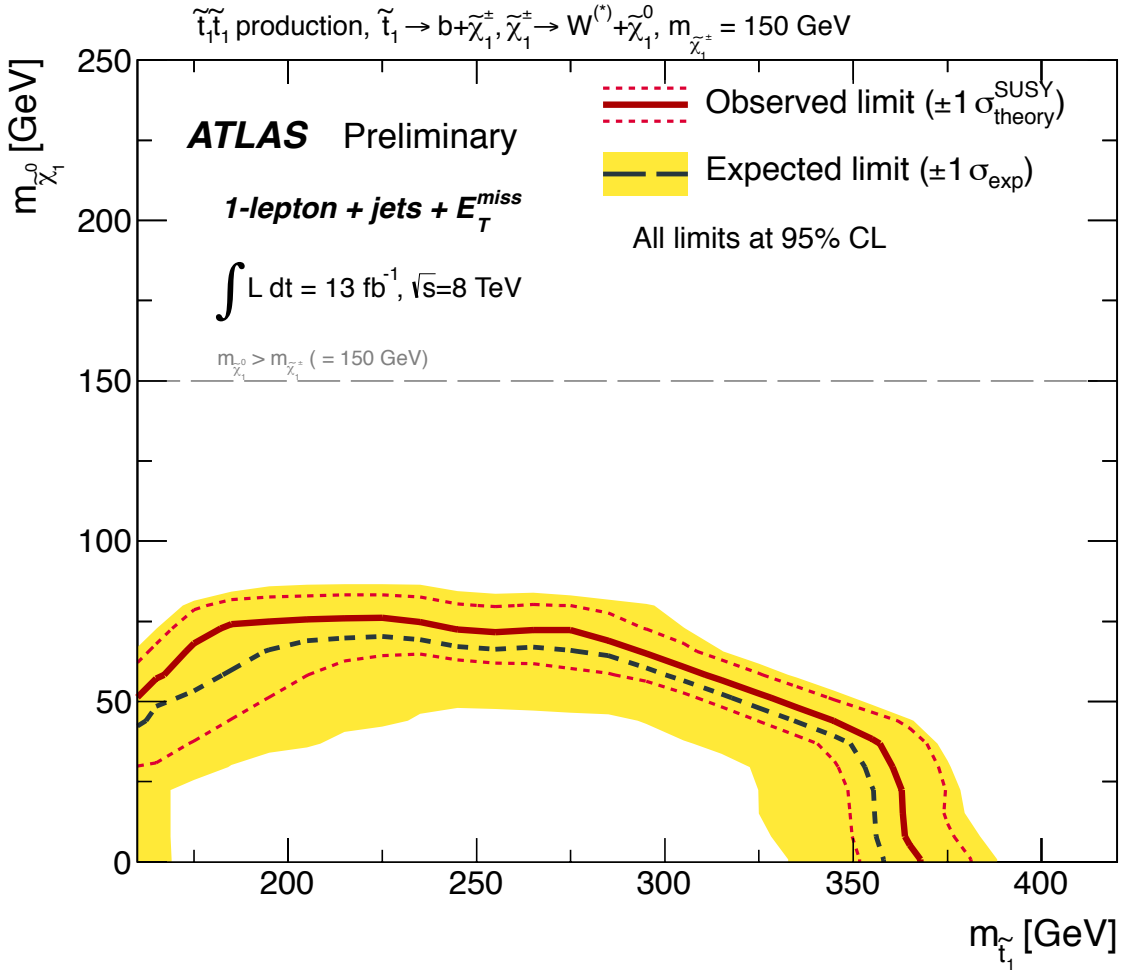

Figure 5: Expected (black dashed) and observed (red solid) 95% CL excluded region (under the curve) in the plane of $m_{\tilde{\chi}_1^0}$ vs. $m_{\tilde{t}_1}$, assuming $\mathcal{B}(\tilde{t}_1 \rightarrow b\tilde{\chi}_1^{\pm}) = 100\%$, $\mathcal{B}(\tilde{\chi}_1^{\pm} \rightarrow W\tilde{\chi}_1^0) = 100\%$, and $m_{\tilde{\chi}_1^{\pm}} = 150\,\text{GeV}$. All uncertainties except the theoretical signal cross section uncertainties are included. The contours of the yellow band around the expected limit are the $\pm 1\,\sigma$ results. The dotted red lines around the observed limit illustrate the change in the observed limit as the nominal signal cross section is scaled up and down by the theoretical uncertainty.

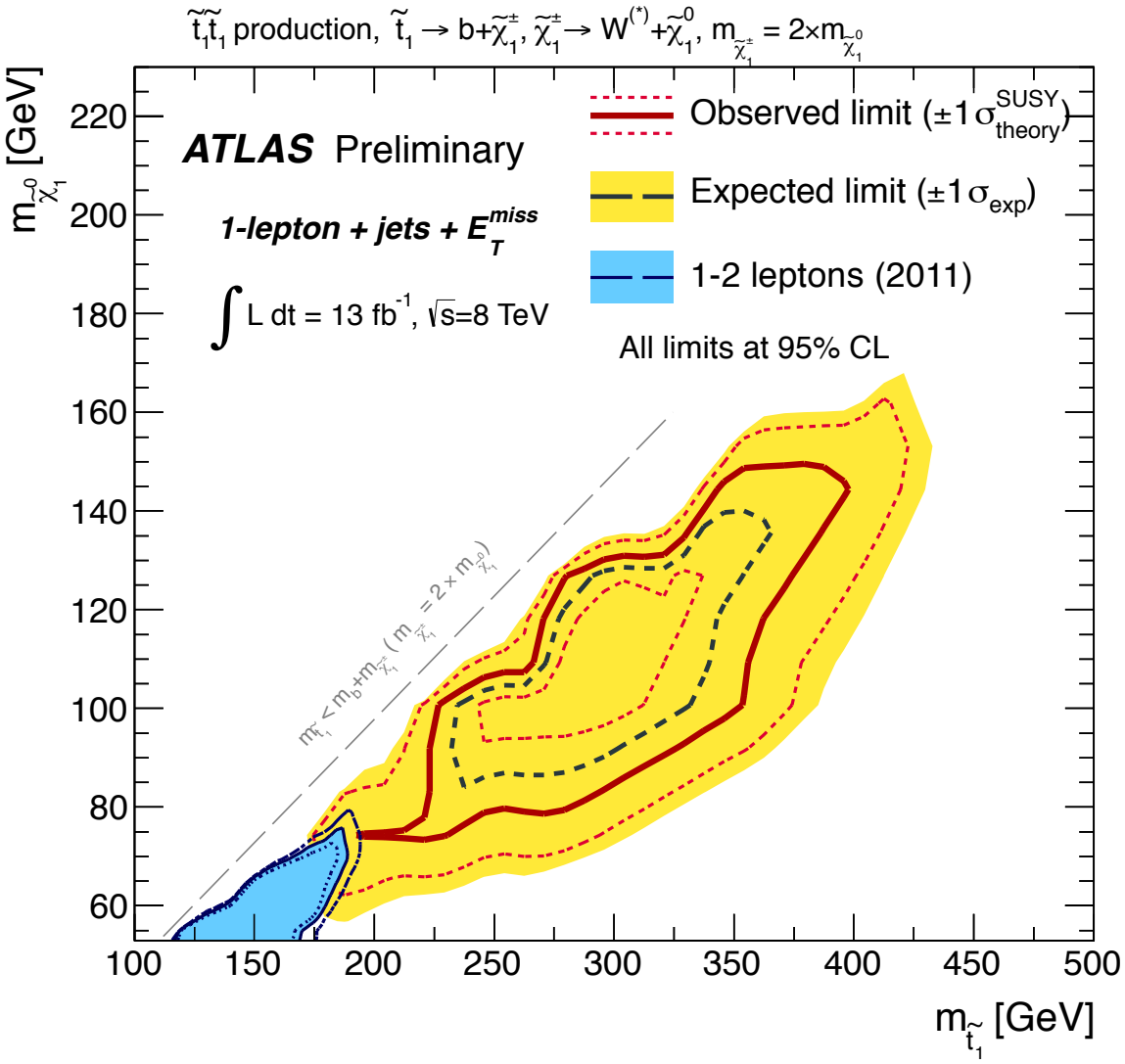

Figure 6: Expected (black dashed) and observed (red solid) 95% CL excluded region (inside the curve) in the plane of $m_{\tilde{\chi}_1^0}$ vs. $m_{\tilde{t}_1}$, assuming $\mathcal{B}(\tilde{t}_1 \to b\tilde{\chi}_1^{\pm}) = 100\%$, $\mathcal{B}(\tilde{\chi}_1^{\pm} \to W\tilde{\chi}_1^0) = 100\%$, and $m_{\tilde{\chi}_1^{\pm}} = 2\times m_{\tilde{\chi}_1^0}$. All uncertainties except the theoretical signal cross section uncertainties are included. The contours of the yellow band around the expected limit are the $\pm 1\,\sigma$ results. The dotted red lines around the observed limit illustrate the change in the observed limit as the nominal signal cross section is scaled up and down by the theoretical uncertainty. For comparison the blue shaded area shows the observed 2011 ATLAS $\tilde{t}_1 \to b\tilde{\chi}_1^{\pm}$ exclusion limit [18], making the same signal assumption ($m_{\tilde{\chi}_1^{\pm}} = 2\times m_{\tilde{\chi}_1^0}$). The dashed and dotted dark blue lines show the corresponding expected and observed $-1\,\sigma^{\rm SUSY}_{\rm theory}$ limits, respectively.

Obs. (exp.) upper limits	SRD	SRE	SRbC	SRtN1	SRtN2	SRtN3
$N_{\text{non-SM}}$	21.3 (16.6)	17.4 (11.5)	70.1 (76.7)	46.0 (40.6)	10.2 (8.1)	10.0 (6.8)
σ_{vis} [fb]	1.6 (1.3)	1.3 (0.9)	5.4 (5.9)	3.5 (3.1)	0.8 (0.6)	0.8 (0.5)

Table 9: Signal model independent upper limits on the number of beyond-SM events ($N_{\text{non-SM}}$) and the visible signal cross section ($\sigma_{\text{vis}} = \sigma_{\text{prod}} \times A \times \epsilon$) in the five signal regions. The numbers (in brackets) give the observed (expected) 95% CL upper limits.

[3] Y. Golfand and E. Likhtman, *Extension of the Algebra of Poincare Group Generators and Violation of p Invariance*, JETP Lett. **13** (1971) 323–326.

[4] A. Neveu and J. Schwarz, *Factorizable dual model of pions*, Nucl. Phys. **B31** (1971) 86–112.

[5] A. Neveu and J. Schwarz, *Quark Model of Dual Pions*, Phys. Rev. **D4** (1971) 1109–1111.

[6] J. Gervais and B. Sakita, *Field theory interpretation of supergauges in dual models*, Nucl. Phys. **B34** (1971) 632–639.

[7] D. Volkov and V. Akulov, *Is the Neutrino a Goldstone Particle?*, Phys. Lett. **B46** (1973) 109–110.

[8] J. Wess and B. Zumino, *A Lagrangian Model Invariant Under Supergauge Transformations*, Phys. Lett. **B49** (1974) 52.

[9] J. Wess and B. Zumino, *Supergauge Transformations in Four-Dimensions*, Nucl. Phys. **B70** (1974) 39–50.

[10] P. Fayet, *Supersymmetry and Weak, Electromagnetic and Strong Interactions*, Phys. Lett. **B64** (1976) 159.

[11] P. Fayet, *Spontaneously Broken Supersymmetric Theories of Weak, Electromagnetic and Strong Interactions*, Phys. Lett. **B69** (1977) 489.

[12] G. R. Farrar and P. Fayet, *Phenomenology of the Production, Decay, and Detection of New Hadronic States Associated with Supersymmetry*, Phys. Lett. **B76** (1978) 575–579.

[13] P. Fayet, *Relations Between the Masses of the Superpartners of Leptons and Quarks, the Goldstino Couplings and the Neutral Currents*, Phys. Lett. **B84** (1979) 416.

[14] S. Dimopoulos and H. Georgi, *Softly Broken Supersymmetry and SU(5)*, Nucl. Phys. **B193** (1981) 150.

[15] R. Barbieri and G. Giudice, *Upper Bounds on Supersymmetric Particle Masses*, Nucl.Phys. **B306** (1988) 63.

[16] B. de Carlos and J. Casas, *One loop analysis of the electroweak breaking in supersymmetric models and the fine tuning problem*, Phys. Lett. B **309** (1993) 320–328.

[17] ATLAS Collaboration, *Search for light scalar top quark pair production in final states with two leptons with the ATLAS detector in* $\sqrt{s} = 7$ *TeV proton-proton collisions*, arXiv:1208.4305 [hep-ex].

[18] ATLAS Collaboration, *Search for light top squark pair production in final states with leptons and b-jets with the ATLAS detector in $\sqrt{s}$ = 7 TeV proton-proton collisions*, arXiv:1209.2102 [hep-ex].

[19] ATLAS Collaboration, *Search for a supersymmetric partner to the top quark in final states with jets and missing transverse momentum at $\sqrt{s}$ = 7 TeV with the ATLAS detector*, Phys. Rev. Lett. **109** (2012) 211802, arXiv:1208.1447 [hep-ex]. http://link.aps.org/doi/10.1103/PhysRevLett.109.211802.

[20] ATLAS Collaboration, *Search for direct top squark pair production in final states with one isolated lepton, jets, and missing transverse momentum in $\sqrt{s}$ = 7 TeV pp collisions using 4.7 fb-1 of ATLAS data*, Phys. Rev. Lett. **109** (2012) 211803, arXiv:1208.2590 [hep-ex]. http://link.aps.org/doi/10.1103/PhysRevLett.109.211803.

[21] ATLAS Collaboration, *Search for a heavy top-quark partner in final states with two leptons with the ATLAS detector at the LHC*, arXiv:1209.4186 [hep-ex].

[22] CMS Collaboration, *Search for direct top squark pair production in events with a single isolated lepton, jets and missing transverse energy at $\sqrt{s}$ = 8 TeV*, CMS-PAS-SUS-12-023, 2012.

[23] CMS Collaboration, *Scalar Top Quark Search with Jets and Missing Momentum in pp Collisions at $\sqrt{s}$ = 7 TeV*, CMS-PAS-SUS-11-030, 2012.

[24] CDF Collaboration, *Search for Pair Production of Supersymmetric Top Quarks in Dilepton Events from $p\overline{p}$ Collisions at sqrt(s)=1.96 TeV*, Phys. Rev. Lett. **104** (2010) 251801.

[25] D0 Collaboration, *Search for the lightest scalar top quark in events with two leptons in ppbar collisions at sqrt(s)=1.96 TeV*, Phys. Lett. **B675** (2009) 289.

[26] ATLAS Collaboration, *Search for supersymmetry using events with three leptons, multiple jets, and missing transverse momentum in 13.0 fb-1 of pp collisions with the ATLAS detector at $\sqrt{s}$ = 8 TeV*, ATLAS-CONF-2012-151, Nov, 2012.

[27] ATLAS Collaboration, *Search for gluino pair production in final states with missing transverse momentum and at least three b-jets using 12.8 fb-1 of pp collisions at $\sqrt{s}$ = 8 TeV with the ATLAS Detector.*, ATLAS-CONF-2012-145, Nov, 2012.

[28] ATLAS Collaboration, *Search for Supersymmetry in final states with two same-sign leptons, jets and missing transverse momentum with the ATLAS detector in pp collisions at $\sqrt{s}$ = 8 TeV*, ATLAS-CONF-2012-105, Aug, 2012.

[29] ATLAS Collaboration, *Search for new phenomena using large jet multiplicities and missing transverse momentum with ATLAS in 5.8 fb^{-1} of $\sqrt{s}$ = 8 TeV proton-proton collisions*, ATLAS-CONF-2012-103, Aug, 2012.

[30] CMS Collaboration, *Search for supersymmetry in final states with missing transverse energy and 0, 1, 2, 3, or at least 4 b-quark jets in 8 TeV pp collisions using the variable AlphaT*, CMS-PAS-SUS-12-028, 2012.

[31] CMS Collaboration, *Search for supersymmetry in hadronic final states using MT2 in pp collisions at $\sqrt{s}$ = 7 TeV*, JHEP **2012** (2012) 1–40.

[32] CMS Collaboration, *Search for supersymmetry in events with same-sign dileptons and b-tagged jets with 8 TeV data*, CMS-PAS-SUS-12-029, 2012.

[33] ATLAS Collaboration, *The ATLAS Experiment at the CERN Large Hadron Collider*, JINST **3** (2008) S08003.

[34] ATLAS Collaboration, *The ATLAS Simulation Infrastructure*, Eur. Phys. J. **C70** (2010) 823–874.

[35] GEANT4 Collaboration, S. Agostinelli et al., *GEANT4: A simulation toolkit*, Nucl. Instrum. Meth. **A506** (2003) 250–303.

[36] ATLAS Collaboration, *The simulation principle and performance of the ATLAS fast calorimeter simulation FastCaloSim*, 2010. ATL-PHYS-PUB-2010-013.

[37] P. Nason, *A New method for combining NLO QCD with shower Monte Carlo algorithms*, JHEP **0411** (2004) 040.

[38] S. Frixione, P. Nason, and C. Oleari, *Matching NLO QCD computations with parton shower simulations: the POWHEG method*, JHEP **0711** (2007) 070.

[39] S. Alioli, P. Nason, C. Oleari, and E. Re, *A general framework for implementing NLO calculations in shower Monte Carlo programs: the POWHEG BOX*, JHEP **1006** (2010) 043.

[40] B. P. Kersevan and E. Richter-Was, *The Monte Carlo event generator AcerMC version 2.0 with interfaces to PYTHIA 6.2 and HERWIG 6.5*, arXiv:hep-ph/0405247 [hep-ph].

[41] ATLAS Collaboration, *Measurement of $t\bar{t}$ production with a veto on additional central jet activity in pp collisions at sqrt(s) = 7 TeV using the ATLAS detector*, arXiv:1203.5015 [hep-ex]. CERN-PH-EP-2012-062.

[42] T. Gleisberg et al., *Event generation with SHERPA 1.1*, JHEP **02** (2009) 007, arXiv:0811.4622.

[43] J. Alwall et al., *MadGraph/MadEvent v4: The New Web Generation*, JHEP **09** (2007) 028.

[44] H.-L. Lai, M. Guzzi, J. Huston, Z. Li, P. M. Nadolsky, et al., *New parton distributions for collider physics*, Phys.Rev. **D82** (2010) 074024.

[45] A. D. Martin, W. J. Stirling, R. S. Thorne, and G. Watt, *Parton distributions for the LHC*, Eur. Phys. J. **C63** (2009) 189.

[46] G. Corcella et al., *HERWIG 6.5: an event generator for Hadron Emission Reactions With Interfering Gluons (including supersymmetric processes)*, JHEP **01** (2001) 010.

[47] J. Pumplin et al., *New generation of parton distributions with uncertainties from global QCD analysis*, JHEP **07** (2002) 012.

[48] T. Sjostrand, S. Mrenna, and P. Z. Skands, *PYTHIA 6.4 Physics and Manual*, JHEP **0605** (2006) 026.

[49] J. M. Butterworth, J. R. Forshaw, and M. H. Seymour, *Multiparton interactions in photoproduction at HERA*, Z. Phys. **C72** (1996) 637–646.

[50] M. Aliev, H. Lacker, U. Langenfeld, S. Moch, P. Uwer, et al., *HATHOR: HAdronic Top and Heavy quarks crOss section calculatoR*, Comput.Phys.Commun. **182** (2011) 1034–1046.

[51] N. Kidonakis, *Next-to-next-to-leading-order collinear and soft gluon corrections for t-channel single top quark production*, Phys.Rev. **D83** (2011) 091503.

[52] N. Kidonakis, *Two-loop soft anomalous dimensions for single top quark associated production with a W- or H-*, Phys.Rev. **D82** (2010) 054018.

[53] N. Kidonakis, *NNLL resummation for s-channel single top quark production*, Phys.Rev. **D81** (2010) 054028.

[54] J. M. Campbell and R. K. Ellis, *$t\bar{t}W^{+-}$ production and decay at NLO*, arXiv:1204.5678 [hep-ph].

[55] R. Gavin, Y. Li, F. Petriello, and S. Quackenbush, *FEWZ 2.0: A code for hadronic Z production at next-to- next-to-leading order*, arXiv:1011.3540 [hep-ph].

[56] J. M. Campbell and R. K. Ellis, *An Update on vector boson pair production at hadron colliders*, Phys.Rev. **D60** (1999) 113006.

[57] J. M. Campbell, R. K. Ellis, and C. Williams, *Vector boson pair production at the LHC*, JHEP **1107** (2011) 018.

[58] M. Bahr et al., *Herwig++ Physics and Manual*, Eur. Phys. J. **C58** (2008) 639–707.

[59] LEP SUSY Working Group (ALEPH, DELPHI, L3, OPAL), Notes LEPSUSYWG/01-03.1 and 04-01.1, http://lepsusy.web.cern.ch/lepsusy/Welcome.html.

[60] W. Beenakker, M. Kramer, T. Plehn, M. Spira, and P. M. Zerwas, *Stop production at hadron colliders*, Nucl. Phys. **B515** (1998) 3–14.

[61] W. Beenakker, S. Brensing, M. Kramer, A. Kulesza, E. Laenen, and I. Niessen, *Supersymmetric top and bottom squark production at hadron colliders*, JHEP. **1008** (2010) 098.

[62] W. Beenakker, S. Brensing, M. Kramer, A. Kulesza, E. Laenen, et al., *Squark and gluino hadroproduction*, Int.J.Mod.Phys. **A26** (2011) 2637–2664.

[63] M. Kramer, A. Kulesza, R. van der Leeuw, M. Mangano, S. Padhi, et al., *Supersymmetry production cross sections in pp collisions at sqrts = 7 TeV*, arXiv:1206.2892 [hep-ph].

[64] ATLAS Collaboration, *Selection of jets produced in proton-proton collisions with the ATLAS detector using 2011 data*, . ATLAS-CONF-2012-020 https://cdsweb.cern.ch/record/1430034.

[65] ATLAS Collaboration, *Studies of the performance of the ATLAS detector using cosmic-ray muons*, Eur. Phys. J. **C71** (2011) 1593.

[66] ATLAS Collaboration. ATLAS-CONF-2011-063 https://cdsweb.cern.ch/record/1345743.

[67] ATLAS Collaboration, *Electron performance measurements with the ATLAS detector using the 2010 LHC proton-proton collision data*, Eur.Phys.J. **C72** (2012) 1909.

[68] M. Cacciari, G. P. Salam, and G. Soyez, *The anti-k_t jet clustering algorithm*, JHEP **04** (2008) 063.

[69] ATLAS Collaboration, *Jet energy measurement with the ATLAS detector in proton-proton collisions at* $\sqrt{s} = 7$ TeV, arXiv:1112.6426 [hep-ex]. CERN-PH-EP-2011-191.

[70] ATLAS Collaboration. ATLAS-CONF-2012-053 http://cdsweb.cern.ch/record/1452641.

[71] ATLAS Collaboration. ATLAS-CONF-2012-063 http://cdsweb.cern.ch/record/1459528.

[72] ATLAS Collaboration. ATLAS-CONF-2012-064 http://cdsweb.cern.ch/record/1459529.

[73] ATLAS Collaboration. ATLAS-CONF-2012-102 http://cdsweb.cern.ch/record/1369219.

[74] ATLAS Collaboration. ATLAS-CONF-2012-040 http://cdsweb.cern.ch/record/1435194.

[75] ATLAS Collaboration. ATLAS-CONF-2012-043 https://cdsweb.cern.ch/record/1435197.

[76] ATLAS Collaboration. ATLAS-CONF-2012-097 http://cdsweb.cern.ch/record/1460443.

[77] C. Lester and D. Summers, *Measuring masses of semiinvisibly decaying particles pair produced at hadron colliders*, Phys.Lett. **B463** (1999) 99–103, arXiv:hep-ph/9906349 [hep-ph].

[78] Y. Bai, H.-C. Cheng, J. Gallicchio, and J. Gu, *Stop the Top Background of the Stop Search*, JHEP **1207** (2012) 110, arXiv:1203.4813 [hep-ph].

[79] A. J. Barr, B. Gripaios, and C. G. Lester, *Transverse masses and kinematic constraints: from the boundary to the crease*, JHEP **0911** (2009) 096, arXiv:0908.3779 [hep-ph].

[80] P. Konar, K. Kong, K. T. Matchev, and M. Park, *Dark Matter Particle Spectroscopy at the LHC: Generalizing M(T2) to Asymmetric Event Topologies*, JHEP **1004** (2010) 086, arXiv:0911.4126 [hep-ph].

[81] ATLAS Collaboration, *Search for supersymmetry in final states with jets, missing transverse momentum and one isolated lepton in* $\sqrt{s} = 7$ *TeV pp collisions using* $1\ fb^{-1}$ *of ATLAS data*, Phys. Rev. D **85** (2012) 012006.

[82] G. Cowan, K. Cranmer, E. Gross, and O. Vitells, *Asymptotic formulae for likelihood-based tests of new physics*, Eur.Phys.J. **C71** (2011) 1554, arXiv:1007.1727 [physics.data-an].

[83] ATLAS Collaboration, *Luminosity Determination in pp Collisions at* $\sqrt{s} = 7$ *TeV Using the ATLAS Detector at the LHC*, Eur.Phys.J. **C71** (2011) 1630.

[84] ATLAS Collaboration. ATLAS-CONF-2011-116 http://cdsweb.cern.ch/record/1376384.

[85] A. Read, *Presentation of search results: the CLs technique*, Journal of Physics G: Nucl. Part. Phys. **28** (2002) 2693–2704.

A Additional plots

The mapping of signal regions SRtN1, SRtN2, and SRtN3 to the $\tilde{t}_1 \rightarrow t\tilde{\chi}_1^0$ signal model is illustrated in Figure 7. The individual exclusion limits of the three SRs is shown in Fig. 8. Figures 9–11 show the exclusion limits as shown in Figures 4–6 together with observed upper limits on the model cross section (per grid point).

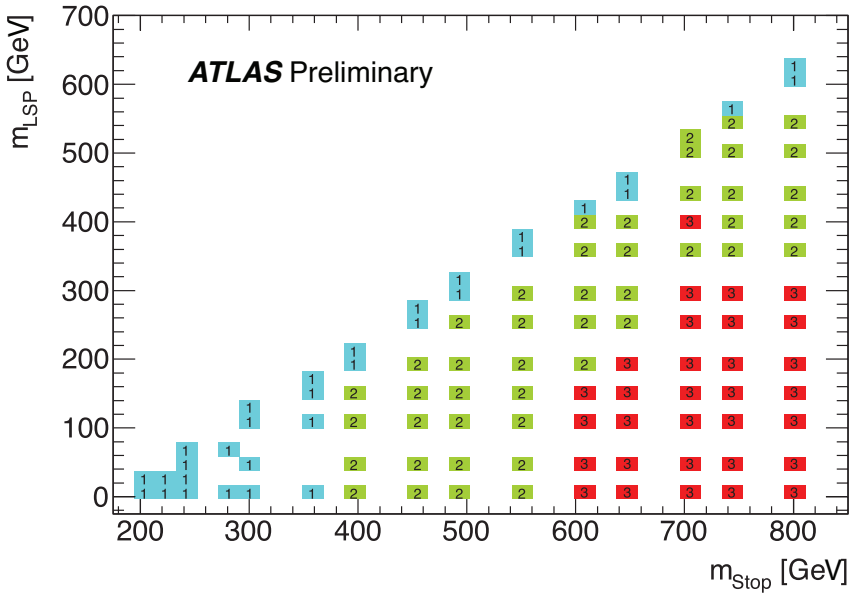

Figure 7: Illustration of the best expected signal region per signal grid point for the stop to top neutralino model, where 1,2, and 3 mean SRtN1, SRtN2, and SRtN3 respectively. This mapping is used for the final combined exclusion limits.

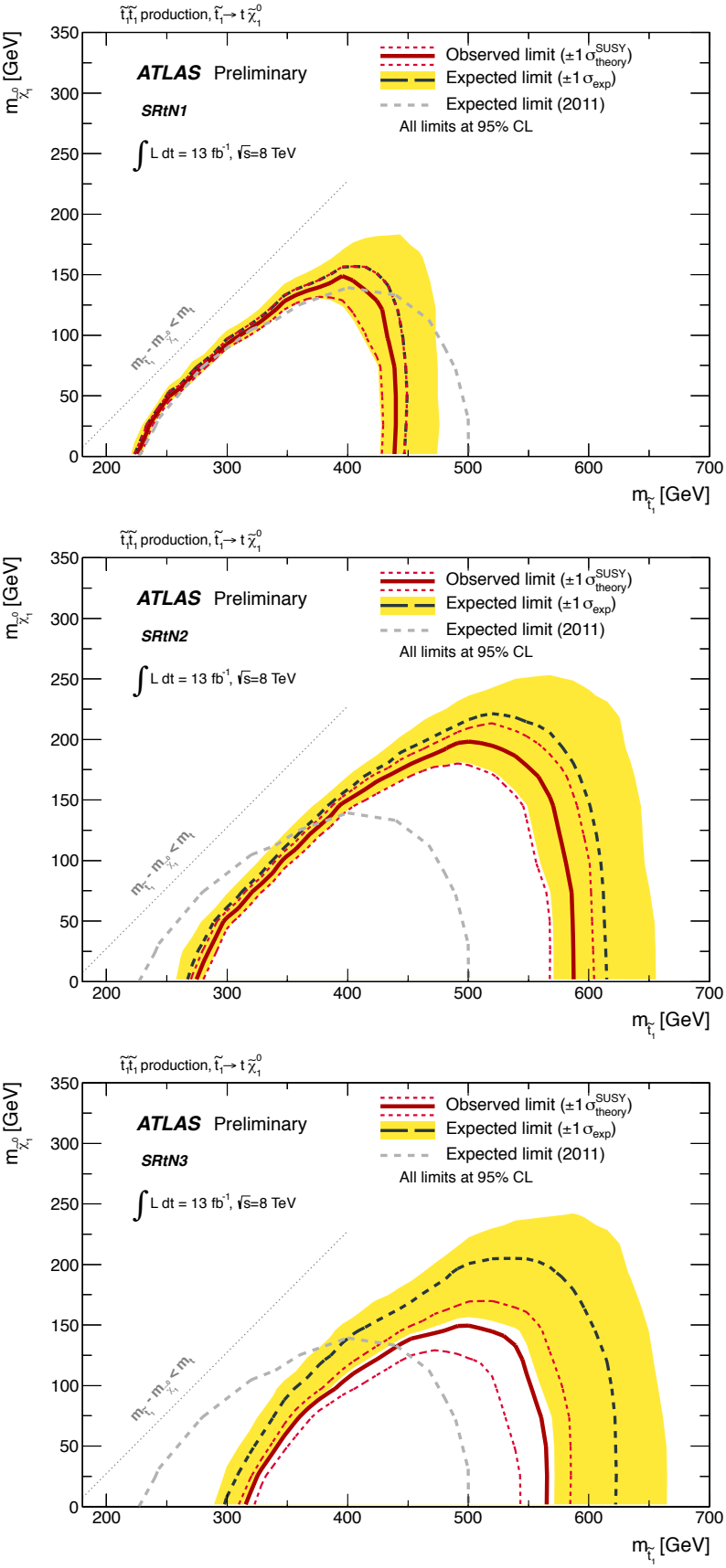

Figure 8: Expected and observed exclusion 95% CL exclusion limits for the three individual signal regions tN1, tN2, and tN3 used in the $\tilde{t}_1 \to t\tilde{\chi}_1^0$ scenario (the excluded region is under the curve).

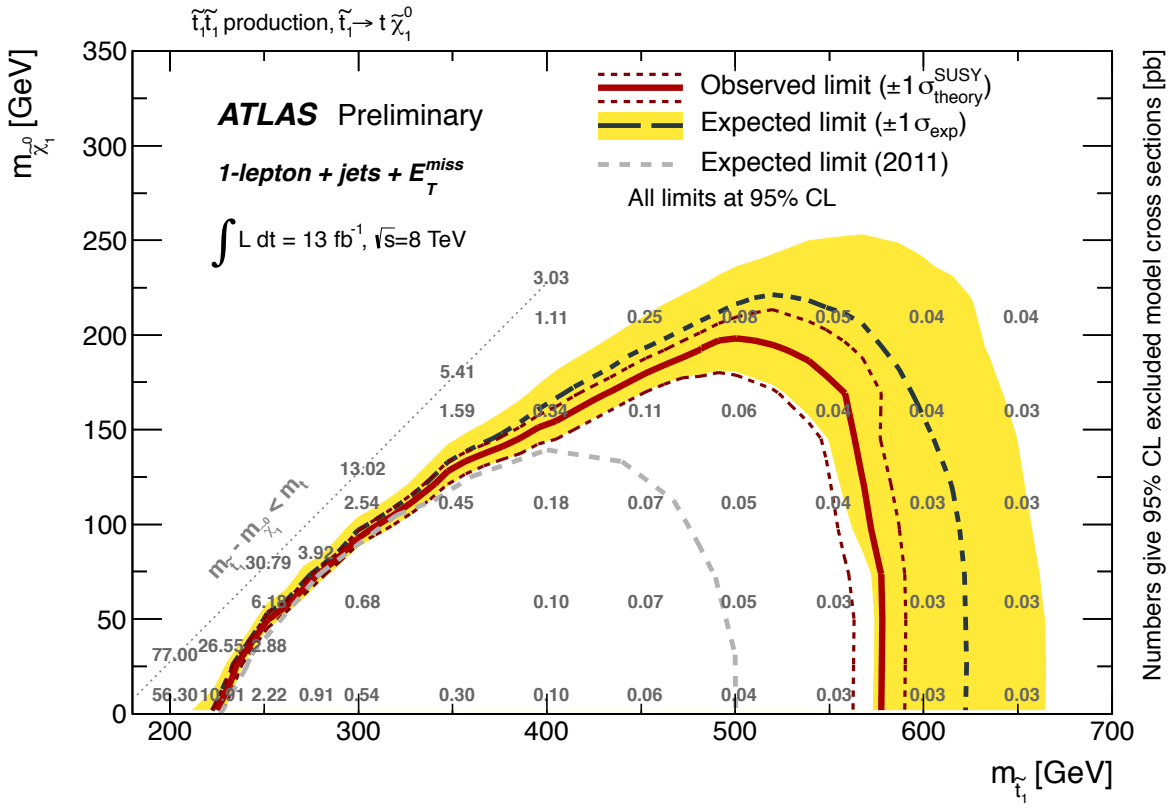

Figure 9: Expected (black dashed) and observed (red solid) 95% CL excluded region (under the curve) in the plane of $m_{\tilde{\chi}_1^0}$ vs. $m_{\tilde{t}_1}$, assuming $\mathcal{B}(\tilde{t}_1 \to t\tilde{\chi}_1^0) = 100\%$. All uncertainties except the theoretical signal cross section uncertainties are included. The contours of the yellow band around the expected limit are the $\pm1\,\sigma$ results. The dotted red lines around the observed limit illustrate the change in the observed limit as the nominal signal cross section is scaled up and down by the theoretical uncertainty. The overlaid numbers give the observed upper limit on the signal cross section, in pb. For improved visibility, these numbers are displayed 10 GeV above the corresponding model points. For comparison the light grey dashed line shows the corresponding 2011 ATLAS expected limit from the stop 1-lepton search [20].

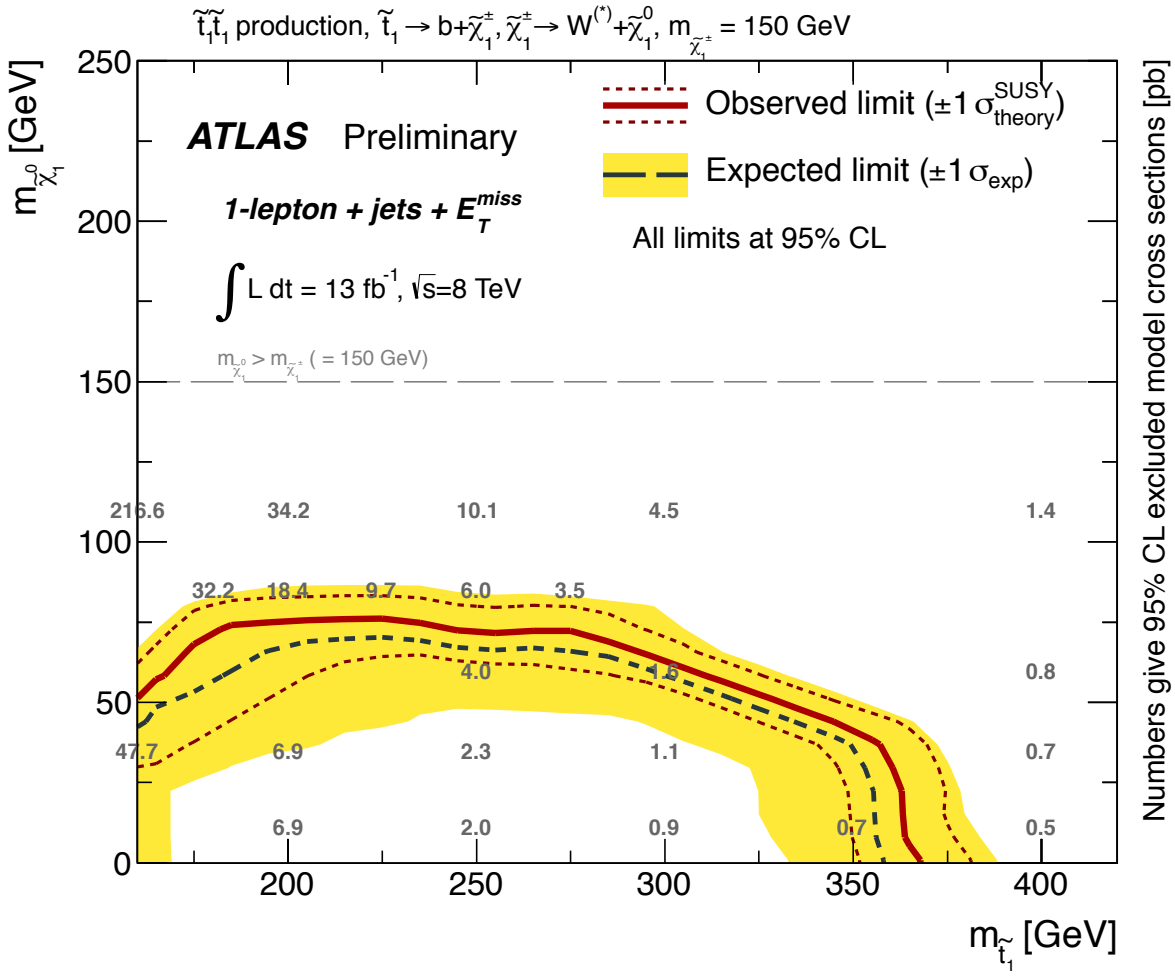

Figure 10: Expected (black dashed) and observed (red solid) 95% CL excluded region (under the curve) in the plane of $m_{\tilde{\chi}_1^0}$ vs. $m_{\tilde{t}_1}$, assuming $\mathcal{B}(\tilde{t}_1 \to b\tilde{\chi}_1^{\pm}) = 100\%$, $\mathcal{B}(\tilde{\chi}_1^{\pm} \to W\tilde{\chi}_1^0) = 100\%$, and $m_{\tilde{\chi}_1^{\pm}} = 150\,\text{GeV}$. All uncertainties except the theoretical signal cross section uncertainties are included. The contours of the yellow band around the expected limit are the $\pm 1\,\sigma$ results. The dotted red lines around the observed limit illustrate the change in the observed limit as the nominal signal cross section is scaled up and down by the theoretical uncertainty. The overlaid numbers give the observed upper limit on the signal cross section, in pb. For improved visibility, these numbers are displayed 10 GeV above the corresponding model points.

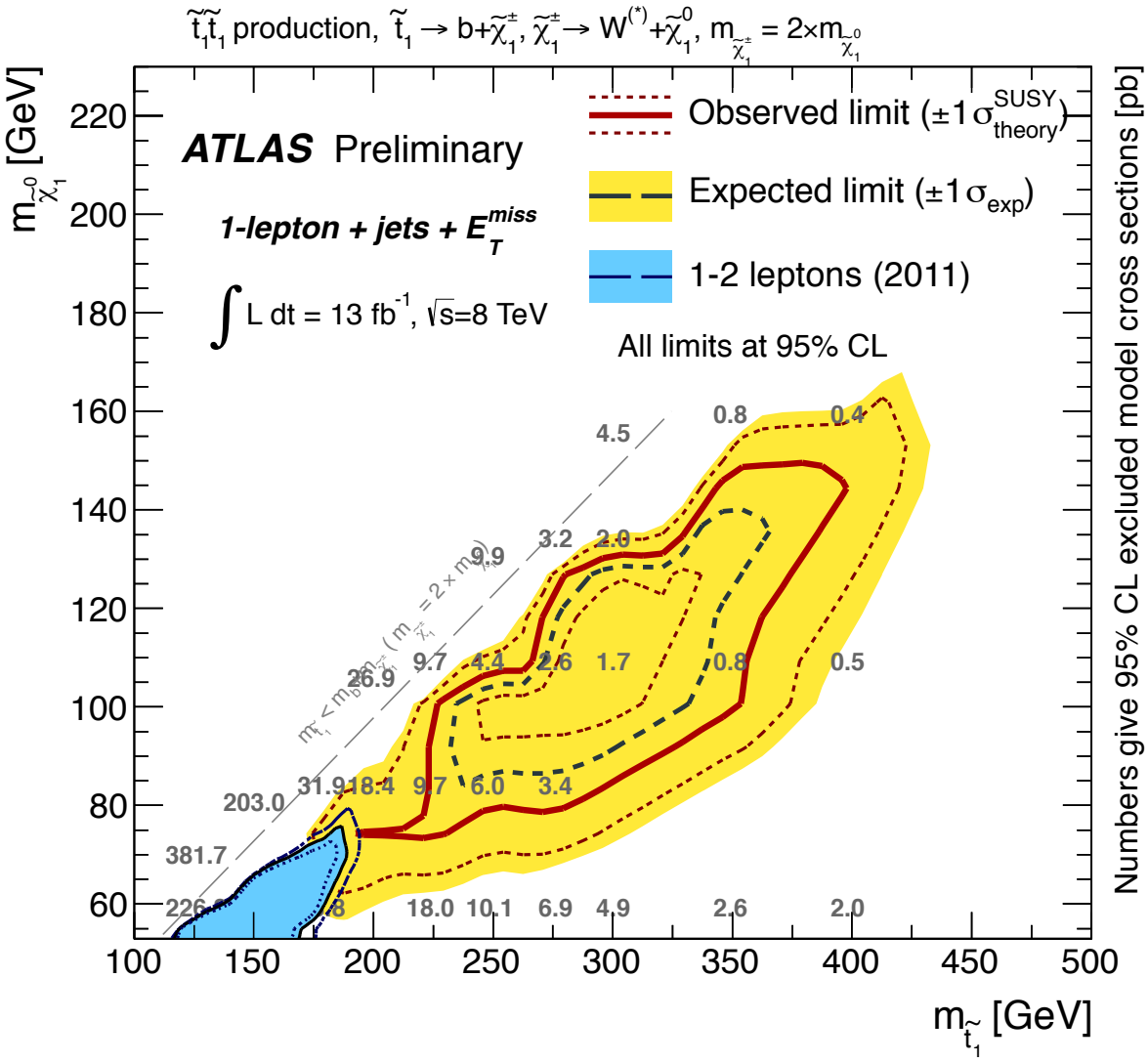

Figure 11: Expected (black dashed) and observed (red solid) 95% CL excluded region (inside the curve) in the plane of $m_{\tilde{\chi}_1^0}$ vs. $m_{\tilde{t}_1}$, assuming $\mathcal{B}(\tilde{t}_1 \rightarrow b\tilde{\chi}_1^{\pm}) = 100\%$, $\mathcal{B}(\tilde{\chi}_1^{\pm} \rightarrow W\tilde{\chi}_1^0) = 100\%$, and $m_{\tilde{\chi}_1^{\pm}} = 2 \times m_{\tilde{\chi}_1^0}$. All uncertainties except the theoretical signal cross section uncertainties are included. The contours of the yellow band around the expected limit are the $\pm 1\,\sigma$ results. The dotted red lines around the observed limit illustrate the change in the observed limit as the nominal signal cross section is scaled up and down by the theoretical uncertainty. The overlaid numbers give the observed upper limit on the signal cross section, in pb. For improved visibility, these numbers are displayed 10 GeV above the corresponding model points. For comparison the blue shaded area shows the observed 2011 ATLAS $\tilde{t}_1 \rightarrow b\tilde{\chi}_1^{\pm}$ exclusion limit [18], making the same signal assumption ($m_{\tilde{\chi}_1^{\pm}} = 2 \times m_{\tilde{\chi}_1^0}$). The dashed and dotted dark blue lines show the corresponding expected and observed $-1\,\sigma^{\text{SUSY}}_{\text{theory}}$ limits, respectively.

B Cut flow for selected benchmark points

Selection name	Electron channel		Muon channel	
	raw counts	events (L=13 fb^{-1})	raw counts	events (L=13 fb^{-1})
No cuts	100000		100000	
Trigger	85808		85484	
All cleaning	84442		84136	
1 lepton	10784	121.7	11588	130.3
4 jets	5963	66.3	6229	69.9
b-jet	5140	57.2	5350	60.5
SRD	817	9.4	862	9.5
SRE	472	5.3	489	5.4
SRtN1	796	8.8	808	8.9
SRtN2	465	5.5	460	5.1
SRtN3	296	3.6	301	3.3
SRbC	1573	17.2	1606	17.8

Table 10: Cut flow for the $\tilde{t}_1 \to t\tilde{\chi}_1^0$ benchmark model with $m_{\tilde{t}} = 500\,\text{GeV}$, and $m_{\tilde{\chi}_1^0} = 200\,\text{GeV}$.

Selection name	Electron channel		Muon channel	
	raw counts	events (L=13 fb^{-1})	raw counts	events (L=13 fb^{-1})
No cuts (1L filtered)	150000		150000	
Trigger	106986		106511	
All cleaning	105221		104773	
1 lepton	27946	1086.3	30282	1205.5
4 jets	8121	314.9	8183	322.9
b-jet	6226	241.8	6142	240.7
SRD	239	8.5	211	8.0
SRE	93	3.1	98	3.5
SRtN1	511	19.7	452	17.9
SRtN2	67	2.2	68	2.6
SRtN3	26	0.9	25	1.0
SRbC	938	36.1	852	33.7

Table 11: Cut flow for the $\tilde{t}_1 \to b\tilde{\chi}_1^{\pm}$ benchmark model with $m_{\tilde{t}} = 350\,\text{GeV}$, $m_{\tilde{\chi}_1^{\pm}} = 300\,\text{GeV}$, and $m_{\tilde{\chi}_1^0} = 150\,\text{GeV}$. This sample was generated with a ≥ 1 lepton filter, yielding a selection efficiency of 55%. All events in the cut flow above passed this generator filter.